ResearchGate

See discussions, stats, and author profiles for this publication at: https://www.researchgate.net/publication/51774340

Dynamics of catalytic tubular microjet engines: Dependence on geometry and chemical environment

Article *in* Nanoscale · November 2011

DOI: 10.1039/c1nr10840a · Source: PubMed

CITATIONS
46

READS
125

6 authors, including:

Jinxing Li
University of California, San Diego
12 PUBLICATIONS **163** CITATIONS
SEE PROFILE

Menglin Li
Fudan University
6 PUBLICATIONS **84** CITATIONS
SEE PROFILE

Ran Liu
Fudan University
224 PUBLICATIONS **1,708** CITATIONS
SEE PROFILE

Some of the authors of this publication are also working on these related projects:

MRS Proceedings View project

NEXT conference series View project

All content following this page was uploaded by Jinxing Li on 21 May 2014.

The user has requested enhancement of the downloaded file.

View Article Online / Journal Homepage / Table of Contents for this issue
Dynamic Article Links

Nanoscale

Cite this: *Nanoscale*, 2011, **3**, 5083

www.rsc.org/nanoscale

PAPER

Dynamics of catalytic tubular microjet engines: Dependence on geometry and chemical environment†

Jinxing Li,‡[ab] Gaoshan Huang,‡*[a] Mengmeng Ye,[b] Menglin Li,[a] Ran Liu*[b] and Yongfeng Mei*[a]

Received 15th July 2011, Accepted 21st September 2011
DOI: 10.1039/c1nr10840a

Published on 07 November 2011 on http://pubs.rsc.org | doi:10.1039/C1NR10840A
Downloaded by University of California - San Diego on 24 February 2013

Strain-engineered tubular microjet engines with various geometric dimensions hold interesting autonomous motions in an aqueous fuel solution when propelled by catalytic decomposition of hydrogen peroxide to oxygen and water. The catalytically-generated oxygen bubbles expelled from microtubular cavities propel the microjet step by step in discrete increments. We focus on the dynamics of our tubular microjets in one step and build up a body deformation model to elucidate the interaction between tubular microjets and the bubbles they produce. The average microjet velocity is calculated analytically based on our model and the obtained results demonstrate that the velocity of the microjet increases linearly with the concentration of hydrogen peroxide. The geometric dimensions of the microjet, such as length and radius, also influence its dynamic characteristics significantly. A close consistency between experimental and calculated results is achieved despite a small deviation due to the existence of an approximation in the model. The results presented in this work improve our understanding regarding catalytic motions of tubular microjets and demonstrate the controllability of the microjet which may have potential applications in drug delivery and biology.

1. Introduction

One of the most inspiring challenges in nanotechnology is to fabricate artificial nanomotors to power nanomachines and nanofactories. Nature has formed a variety of sophisticated and perfect systems fuelled with chemical energy, and well-controlled nanomachines can execute translational and rotational movement precisely.[1,2] They effectively utilize the chemical energy released from spontaneous reactions of energy-rich biomolecules, such as the hydrolysis of adenosine triphosphate,[3] to perform various mechanical functions in the micro-/nano-world. The outstanding performance of these biomotors in nature has stimulated interest in fabrication of man-made micro-/nano-motors which can mimic the behaviors of biomotors to operate in locally-supplied chemical fuels and achieve various functions. For instance, researchers have developed the first generation of catalytic motors on the micro-/nano-scale which exhibit autonomous self-propulsion in the presence of hydrogen peroxide.[4–6] The catalytic micro-/nano-motors which move autonomously by deriving chemical energy directly from nearby environment are highly attractive for potential applications in the pharmaceuticals industry and in biology, *e.g.* drug delivery, surgical operation, liquid agitation *in vivo*, and biosensing.[7,8]

Understanding the propulsion mechanism of catalytic micro-/nano-motors is of great significance in both fundamental research and practical applications for designing micro-/nano-machines. Though the basic chemical reactions therein are well-known, there is no consensus in the literature on the dynamics and the movement behaviors of micro-/nano-objects which are self-propelled catalytically. The issue becomes more complicated since the mechanism responsible for self-propulsion depends on not only the nature, but also the dimensions and the architecture of micro-/nano-motors. Several mechanisms have previously been proposed for the self-propulsion of catalytic nanomotors, including "non-bubble-recoiling" mechanisms such as Brownian diffusiophoreis,[9] interfacial tension,[5] and self-electrophoresis.[10] The Brownian diffusiophoresis model is based on the idea that the oxygen generated at one end of bimetalic (Au/Pt or Au/Ni) nanorods decreases the viscosity in the vicinity, enabling thermal motion in that direction. The other two models predict the movement in the opposite direction.[5,10] Different from those "non-bubble-recoiling" mechanisms, the oxygen-bubble-induced gravitational force mechanism states that the bubble formation and the gravitational force are responsible for the hydrodynamic behavior of the monocomponent platinum nanorods.[11] Another "bubble-recoiling" mechanism based on the dynamics of bubble growth and detachment proposes that the propelling force is

[a]*Department of Materials Science, Fudan University, Shanghai, 200433, People's Republic of China. E-mail: gshuang@fudan.edu.cn; yfm@fudan.edu.cn; Fax: +86-21-6564 3615; Tel: +86-21-65642829*
[b]*State Key Lab of ASIC and System, Fudan University, Shanghai, 200433, People's Republic of China. E-mail: rliu@fudan.edu.cn*

† Electronic supplementary information (ESI) available: I. Video of the catalytic motion of a typical microjet moving in a linear way. II. Detailed numerical analyses: Reynolds number calculation, displacement of the microjet and the bubble after separation, and example of experimental velocity calculation. See DOI: 10.1039/c1nr10840a

‡ J.X.L. and G.S.H. contributed equally to this work.

Published on 07 November 2011 on http://pubs.rsc.org | doi:10.1039/C1NR10840A
Downloaded by University of California - San Diego on 24 February 2013

directed away from the catalyst site on a Pt-coated microsphere.[12] However, visualization of the nanobubbles forming and detaching has proven difficult in previous research because the typical bubble dimension is beyond the resolution of conventional microscopy. The interaction of the moving object and the bubble cannot be investigated in a direct manner and is thus still a matter of controversy.

Recent tubular microjet engines with high-speed motions due to bubble recoiling are fabricated using newly-developed technologies.[13,14] The microtubular jet engines demonstrate advanced performance and related applications such as high speed,[14] precise motion control,[15] cargo transportation and assembly,[15] biocatalytic propulsion,[16] and dynamic self-assembly,[17] which pave a promising way towards constructing multifunctional and intelligent micro-/nano-motors.[18] The hydrodynamic behaviors of the microjet engines and the microbubbles are similar to that of the micro-sized creatures with asymmetric geometry demonstrating excellent strategies for swimming at low Reynolds numbers through mechanical deformation of their bodies.[19,20] The microscopy visualization of the trajectories of the microjet engines and the microbubble tails they leave behind reveals that the tubular engines thrust forward step by step in discrete increments.[21]

Here we focus on the dynamics of the bubble migration in one step and build up a body deformation model to illustrate the interaction between the bubble and the microjet. It has been found that microjet geometry and the surrounding chemical environment (*e.g.* the geometric parameters of the microtubular cavity, the size and the production rate of the oxygen bubbles, and the solution concentration), dominantly determine the hydrodynamic behavior of the microjet. Our results indicate that the velocity increases linearly with the concentration of the chemical fuel, and a strong dependence of the velocity of the microjet upon its length and radius was also seen. The validity of the model is proven by fitting closely with our experimental results. Interestingly, their speed by body length in one second exhibits a different dependence on their geometry than when focusing purely on absolute speed alone.

2. Experimental procedures

Catalytic microtubular jet engines with various lengths and diameters are designed by rolling up strained metallic nanomembranes through selectively etching the sacrificial polymer. The lift off resist (LOR, based on polymethylglutarimide (PMGI)), delivered by the MicroChem Ltd, is used as the sacrificial resist layer because its dissolvability in alkaline chemicals and inertia in most organic solvents facilitate patterning the upper layers through photolithography and lift-off process.[22] On a Si substrate, the LOR layer with a thickness of 2 μm was initially spin-coated and then pre-baked at 180 °C for 20 min. A photoresist layer (RFJ-220) was then lithographically patterned on the LOR layer. Strained Pt/Co/Ti metal films were deposited at 100 °C by magnetron sputtering at a pressure of 5×10^{-5} Pa. After a lift-off process, metal films with square patterns were left on the LOR layer. The LOR layer was then selectively dissolved by a dilute KOH solution, allowing the release of the deposited metallic multi-layers. As a result, the planar metal layer rolled up into a tubular-scroll.[21,23] The radius of the tubular cavity can be tuned by changing the thickness of the metal layers. The microtube with radius of 5, 10, 16, and 23 μm are obtained by using the Ti/Co/Pt system with thickness of 10/10/5, 15/15/5, 20/20/5, and 25/25/5 nm, respectively. The length is controlled by predefining lithography patterns (*e.g.* 50 × 50, 70 × 70, 100 × 100, 150 × 150, 200 × 200, and 400 × 400 μm^2). Aqueous H_2O_2 solutions with different concentrations are used as chemical fuels for the catalytic microjets. The images and the live videos with a rate of 20 frames/s of the catalytic microjet motion were captured by a Keyence VHX-600 optical microscope. The velocity was obtained by tracking the trajectories of microjets recorded in the video. Each experimental velocity value represents the average of the velocities for 5 microjets taken over a certain time interval.

3. Results and discussion

Fig. 1a and 1b show two typical motion trajectories of the catalytic tubular microjets: relatively linear (see also the video in the ESI†) and circular. The autonomous motion of the catalytic microjets is the result of the localized chemical reaction, $2H_2O_2 = 2H_2O + O_2$. The decomposition of hydrogen peroxide is catalytically accelerated by the Pt on the inner surface of the microtube and the produced oxygen then coalesces into bubbles. Fig. 1c schematically shows the bubble production and migration process inside the tubular cavity of the microjet: bubbles nucleate upon the decomposition of H_2O_2 induced by the catalytic Pt and move to one opening of the cavity. Due to imperfections in the tubular structure, the bubbles may be ejected in certain directions,[13] and the corresponding recoiling force leads to motion of the microjet in the opposite direction. Unlike Ozin's bimetallic rod-based nanomotors and Zhao's spherical microparticle-based motors where the gas is produced at the outer catalytic surface,[6,24] the oxygen is produced in our case by the fast reaction on the inner catalytic surface and is collected by the tubular cavity. The relatively large size of the cavity causes the produced oxygen to develop into bubbles with sizes in the micrometre range and thus can easily be visualized by ordinary optical microscopy.

The bubbles ejecting from the catalytic microjet propel the jet step by step and each bubble pushes the jet forward by one step

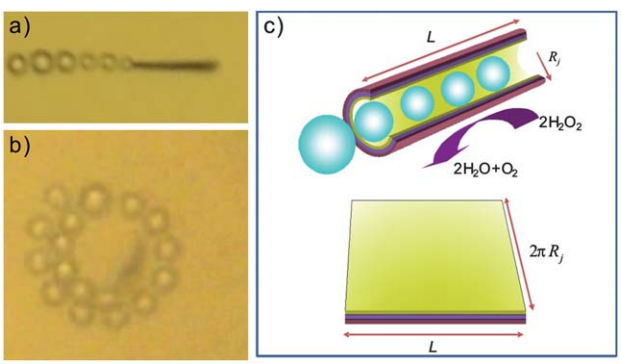

Fig. 1 Typical motion trajectories of the microjet engines: (a) relatively linear and (b) circular. (c) An open view of bubble formation and migration inside the microtube and the corresponding schematic diagram of the inner surface area of the rolled-up microtube.

This journal is © The Royal Society of Chemistry 2011

Published on 07 November 2011 on http://pubs.rsc.org | doi:10.1039/C1NR10840A
Downloaded by University of California - San Diego on 24 February 2013

length.[21] In our previous study, we found that the average step length of the microjet is approximately equal to the bubble radius and the average microjet velocity is equal to the product of the bubble radius and expelling frequency if the microjet moves along a linear trajectory.[13] However, the equations are deduced directly from experimental results and the relation obtained is still phenomenological and empirical. To figure out what the microjet velocity depends on, we must quantitatively determine the bubble generation frequency and the average moving step length caused by the bubble ejection. One may infer that the bubble expelling frequency depends upon the production rate of oxygen and the bubble size.[11] The production rate can be determined experimentally by measuring the volume of the produced oxygen from a planar Pt surface with the area predefined. The result indicates that the productivity of oxygen is linearly proportional to the area of Pt surface S and the H_2O_2 concentration $C_{H_2O_2}$. As illustrated in Fig. 1c, for a tubular cavity with a radius of R_j and a length of L, the inner Pt surface area is $S = 2\pi R_j L$. The oxygen productivity can be expressed as

$$k = dV_{O_2}/dt = nC_{H_2O_2}S = nC_{H_2O_2}2\pi R_j L \quad (1)$$

where n is a rate constant experimentally estimated to be $\sim 9.8 \times 10^{-4}$ m s^{-1} from both flat and rolled surfaces in H_2O_2 with concentrations up to $\sim$10%. The bubble expelling frequency is thus deduced using average bubble radius R_b:

$$f = \frac{nC_{H_2O_2}2\pi R_j L}{V_{\text{bubble}}} = \frac{nC_{H_2O_2}2\pi R_j L}{4\pi R_b^3/3} = \frac{3nC_{H_2O_2}R_j L}{2R_b^3} \quad (2)$$

This suggests that f bubbles are expelled from the microjet in one second, and correspondingly, the bubbles propel the microjet f steps forward.

To quantitatively determine the step length and the velocity of the microjet during catalytic motion, we focus on the dynamics of the ejection process of one bubble and build up a body deformation model to illustrate the interaction between the bubble and the microjet. In our model the microjet and the bubble are considered to be one system which shows geometric asymmetry and flexibility of the configuration. When the microjet-bubble system make a cyclic and asymmetric body change from "microjet with a bubble inside" into "microjet with a detached bubble", the microjet thrusts and obtains the autonomous motion at low Reynolds numbers (see ESI†). The body deformation model is schematically illustrated in Fig. 2 and can be divided into several stages. Firstly, the catalytic reaction in the cavity produces an oxygen bubble in the cavity and the pressure therein propels the bubble to migrate along the long axis to the opening (stage 1). It is worth noting that our experimental observation reveals that the bubble nucleation and growth in the tubular cavity does not generate driving force along the tube axis. The microjet thrusts only when the accumulated gas bubbles are squeezed out of the tubular cavity through the opening.[13] Therefore the initial time point ($t = t_0$) is set as the system demonstrates stage 1. In our model after t_0, we consider the bubble to migrate with a velocity of $\vec{v}_b(t)$ caused by the pressure in the cavity, and push the microjet to move in opposite direction with a velocity of $\vec{v}_j(t)$ (stage 2). Our experimental observation demonstrates that the microjet-bubble system is initially at rest while the bubble and the microjet move in opposite directions

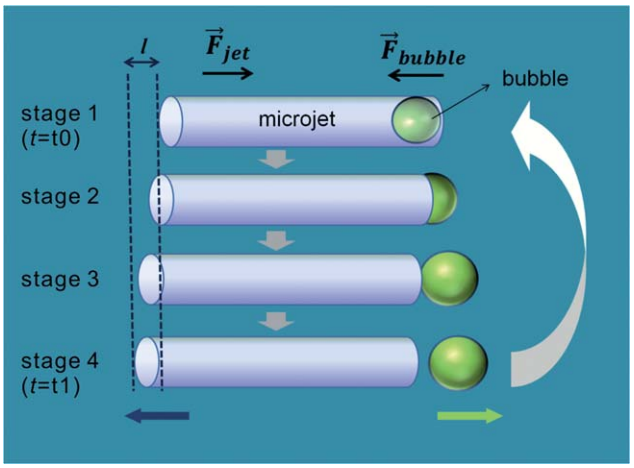

Fig. 2 Schematic diagram of the microjet-bubble system deformation process in one moving step. The microjet-bubble system makes a cyclic and asymmetric change from "microjet with a bubble inside" (stage 1) into "microjet with a detached bubble" (stage 4) which causes the motion of the microjet. In this moving process, the microjet moves forwards at a velocity of $\vec{v}_j(t)$ and the bubble moves backwards at a velocity of $\vec{v}_b(t)$. The drag forces acting on the microjet and the bubble are $\vec{F}_{\text{jet}}$ and $\vec{F}_{\text{bubble}}$ respectively. The separation in stage 4 is exaggerated for the sake of clarity.

with increasing velocities during this stage. The bubble, which is attached to the end of the microjet, continues to move until the moment of separation (stage 3). The detached bubble and the microjet drift with momentum gained and slow down, and a decrease in both $\vec{v}_b(t)$ and $\vec{v}_j(t)$ can thus be observed with different ramp rates. The drag forces on the microjet ($\vec{F}_{\text{jet}}$) and bubble ($\vec{F}_{\text{bubble}}$) finally decrease $\vec{v}_b(t)$ and $\vec{v}_j(t)$ to zero respectively and the system evolves to stage 4 ($t = t_1$), and the movement in one step is accomplished. During the whole body deformation process, the microjet moves forwards and the bubble moves backwards. The process cycles to achieve continuous movement in steps, and linear motion of the microjet is thus observed. One can see that the locomotion strategy of catalytic microjets is similar to that of the low Reynolds numbers swimmers, *e.g. Escherichia coli*, which moves in liquid by mechanical deformation of their body.[19,25] Here, we should also point out that slight expansion of the bubble volume caused by the balance of the gas pressure and the liquid surface tension could exist after expelling (from stage 2 to stage 4),[26] but for the sake of simplicity we will assume that every bubble retains its shape and holds a constant equivalent radius R_b which causes the same step length in each step. The approximation used in our model makes the analytical calculation feasible and will be validated by experimental results (see below). The size of the bubble is sketched to be the same as the diameter of the tubular microjet in Fig. 2 as an example, however, the real situation is not so easy and the size of the bubble is normally larger, since bubble volume expansion exists after expelling from the opening (as displayed in Fig. 1a and 1b). This will be taken into consideration during calculation and discussed in more detail later.

The motion of the microjet in the whole body deformation process can be analyzed using the principles of momentum. For the whole microjet-bubble system, all the external forces that need to be considered are $\vec{F}_{\text{bubble}}$ and $\vec{F}_{\text{jet}}$, which act on the

Published on 07 November 2011 on http://pubs.rsc.org | doi:10.1039/C1NR10840A
Downloaded by University of California - San Diego on 24 February 2013

bubble and the microjet, respectively. Therefore, the change in momentum of the whole system is equal to the integral of resultant force of all external forces with respect to the time applied:

$$\int_{t_0}^{t_1}\vec{F}_{\text{bubble}}dt+\int_{t_0}^{t_1}\vec{F}_{\text{jet}}dt=m_b(\vec{v}_b(t_1)-\vec{v}_b(t_0))+m_j(\vec{v}_j(t_1)-\vec{v}_j(t_0)) \quad (3)$$

where m_b is the average mass of the bubble and m_j the mass of the microjet. For the motion at the microscale, Stokes's law should be utilized to estimate the value of $\vec{F}_{\text{bubble}}$:[27]

$$\vec{F}_{\text{bubble}}=-6\pi\mu R_b\vec{v}_b(t) \quad (4)$$

where R_b is the bubble radius and μ is the fluid viscosity. Assuming the tubular cavity is a cylindrical structure filled with oxygen, $\vec{F}_{\text{jet}}$ is parallel to the tube surface and can be approximated as

$$\vec{F}_{\text{jet}}=-\frac{2\pi\mu L\vec{v}_j(t)}{\ln\left(\frac{2L}{R_j}\right)-0.72} \quad (5)$$

where L is the length and R_j is the radius of the tube.[27]

It is worth noting that in eqn (3), $\vec{v}_b(t_0)$ and $\vec{v}_j(t_0)$ are the velocities of the bubble and the microjet at the initial time point t_0, respectively. As we mentioned in our above model, the bubble nucleation inside the tubular cavity does not contribute to the movement of the bubble and the microjet, *i.e.* the bubble and the microjet are at rest at $t=t_0$ and thus we have $\vec{v}_b(t_0)=0$ and $\vec{v}_j(t_0)=0$. Also, as suggested by the model, both moving objects are hindered by the drag forces and finally stopped, and thus we get $\vec{v}_b(t_1)=0$ and $\vec{v}_j(t_1)=0$. Therefore, for linear movement, the momentum equation (eqn (3)) of our model is simplified as

$$\int_{t_0}^{t_1}\vec{F}_{\text{bubble}}dt+\int_{t_0}^{t_1}\vec{F}_{\text{jet}}dt=0 \quad (6)$$

For our microjet moving in the water at a speed of hundreds of microns per second, the Reynolds number is very low ($\sim10^{-2}$, see ESI†). In this case, the viscosity forces dominate the motion and the inertia of the objects is no longer important.[24] The microjet moves for as long as the driving force (bubble recoiling) acts. We found that the displacement of the bubble and the microjet after separation is in the range of nanometres because of the acting drag force (see ESI†), and thus can be neglected in our calculation. Therefore, for the whole movement cycle (the microjet-bubble system changing its shape from stage 1 to stage 4), the bubble and the microjet are separated with a distance of $2R_b$, which is the sum of the displacements of the microjet and the bubble:

$$2R_b=\int_{t_0}^{t_1}\vec{v}_j(t)dt+\int_{t_0}^{t_1}\vec{v}_b(t)dt \quad (7)$$

Combining eqn (4), (5), (6), and (7), we obtain the displacement of the microjet l in one step:

$$l=\int_{t_0}^{t_1}v_j(t)dt=\frac{6R_b^2}{3R_b+L/\left(\ln\left(\frac{2L}{R_j}\right)-0.72\right)} \quad (8)$$

Based on eqn (2), we may infer that the average velocity of the microjet v_j^{ave}, *i.e.* the total length of f steps, can be written as:

$$v_j^{\text{ave}}=f\times l=\frac{9nC_{H_2O_2}R_jL}{3R_b^2+LR_b/\left(\ln\left(\frac{2L}{R_j}\right)-0.72\right)} \quad (9)$$

Eqn (9) predicts that the average microjet velocity v_j^{ave} is linearly proportional to the hydrogen peroxide concentration $C_{H_2O_2}$ and also depends upon the microjet length L, microjet radius R_j, and bubble size R_b. This equation indicates that the catalytic motion of microjets in the H_2O_2 solution is complex, and the velocity is influenced by several experimental parameters, especially the microjet geometry and the chemical environment. To go deeper into the dynamics of the catalytic motion of our microjet, eqn (9) will be discussed in more detail and the experimental results will also be presented for comparison in the following paragraphs.

The dependence of the microjet velocity v_j^{ave} on the radius of microjet R_j is shown in Fig. 3, where v_j^{ave} for microjet in 5% H_2O_2 is calculated with a length L of 100 μm and radius R_j ranging from 5 to 25 μm. It is worth noting that from our observation, the equivalent bubble radius R_b should be larger than the radius of the microjet R_j, and we experimentally found that R_b was proportional to R_j. To illustrate the influence of bubble radius on the microjet velocity, different bubble radii with values ranging from R_j to $1.5R_j$ are adopted in calculation using eqn (9), and the obtained results are plotted in Fig. 3 using solid lines. For comparison we measured the velocities of microjets with different geometries and the results are also shown, as the square symbols in Fig. 3. Each experimental point represents the average of the velocities for five microjets (ESI†). The overlap between experimental and calculated results proves that R_b is indeed slightly larger than R_j. Moreover, the experimental result of the microjets with radius of 5 μm fits well with calculated curve of $R_b=1.4R_j$ while for the bigger microjets (larger R_j), the experimental results fit with the $R_b=1.1R_j$ curve from calculation. The difference implies case-dependent volume expansions of the bubbles expelled from microtubular cavities with different

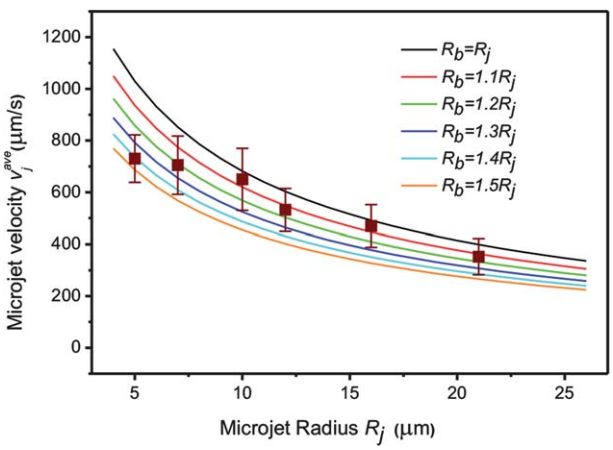

Fig. 3 Dependence of average microjet velocity v_j^{ave} on microjet radius R_j. v_j^{ave} is calculated for microjets with radii R_j ranging from 5 to 25 μm and a uniform length of $L=100$ μm. The H_2O_2 concentration $C_{H_2O_2}$ is 5%. The solid curves represent bubble radii R_b with values from R_j to $1.5R_j$. The square symbols show v_j^{ave} from our experiment results.

This journal is © The Royal Society of Chemistry 2011

Downloaded by University of California - San Diego on 24 February 2013
Published on 07 November 2011 on http://pubs.rsc.org | doi:10.1039/C1NR10840A

radii. As we know, the bubble expansion mostly depends on the pressure difference between the inner gas and the vicinity. The generated bubbles in the cavity with smaller radii experience a higher pressure than those in the larger microjet because of the relatively smaller volume. Therefore, for microjet with smaller R_j the bubble expands remarkably but for microjet with larger R_j the bubble radius is close to the R_j and this difference can be clearly seen in microscopy observation. Another obvious feature that needs to be stressed in Fig. 3 is that v_j^{ave} decreases with increasing R_j. For larger R_j and correspondingly larger R_b, the bubble expelling frequency f decreases because R_b^3 increases in the denominator of eqn (2). The larger microjet will travel more slowly due to lower f although the average step length l increases with R_b (see eqn (8)).

Eqn (9) demonstrated that v_j^{ave} is also a function of microjet length L, however, the dependence of the microjet dynamics on L is more complex. The solid lines in different colors plotted in Fig. 4 represent the calculated v_j^{ave} for microjets with fixed radius of 10 μm but different R_b, as we discussed before. In the calculation, the $C_{H_2O_2}$ is set to be 7% according to the experiment and L ranging from 50 to 400 μm. The increase of v_j^{ave} as a function of L is noticeable for all the solid lines. The reason is that the longer jet has a longer inner Pt surface, which has a larger surface area and therefore results in higher oxygen production. This, as a consequence, leads to a higher bubble expelling frequency (eqn (2)), making the microjet move faster (see Fig. 4). However, the increase of v_j^{ave} becomes gradually counteracted because the drag force on the microjet F_{jet} also increases with L, which slows down the thrust of the microjet, and correspondingly, the step length in one cycle l is reduced as reflected in eqn (8). The red squares in Fig. 4 represent the experimental results from our optical microscopy, and they can be divided into two regions: (I) $L \leq$ 150 μm; (II) $L \geq 200$ μm. In region I, the experimental results fit in well with the theoretical calculation using eqn (9) when $R_b = 1.1R_j$, verifying the applicability of the equation and our body-deformation model. Unfortunately, in region (II) remarkable deviation between experimental and calculated results is observed due to a dramatic velocity drop in experimental results for $L \geq 200$ μm. The inconsistency is believed to be connected with the structural imperfection in the ultra-long microjet. As one can see from the microscope image displayed in the right inset of Fig. 4, the bubbles are expelled from both openings of an ultra-long microtubular cavity, which was not observed in the case of the shorter microjets and is not considered in our model. The ultra-long microjet results in the situation of very high oxygen production and in this case the accumulated oxygen generates great pressure, causing the bubbles to be expelled from both openings. The interaction between the microjet and the bubbles expelled from the front opening acts to counteract the forward motion of the microjet, and partially balance the driving force in the normal situation, making v_j^{ave} decrease dramatically. We should stress that the expelling of oxygen bubbles from the front opening of the cavity was also observed for catalytic micro-pumps working in a circumstance with very high peroxide concentration.[28] These experimental phenomena suggest that our model, which only considers bubble expulsion from one opening, cannot be applicable to a situation where very long microjets or very high H_2O_2 concentration may lead to bubbles being expelled from both openings due to over-high oxygen production.

Fig. 5 depicts the average velocities v_j^{ave} of microjets with the same geometric dimensions (R_j = 10 μm and L = 100 μm) as a function of H_2O_2 concentration $C_{H_2O_2}$. The relationship is relatively simpler since eqn (9) demonstrates a linear dependence. Our experimental results show that v_j^{ave} increases from 275 to 1180 μm s^{-1} upon raising $C_{H_2O_2}$ from 3 to 10%. The significant increase of the v_j^{ave} with increasing $C_{H_2O_2}$ is illustrated intuitively in the inset picture, which exhibits the displacement of three microjets (during a one second period) in H_2O_2 solution with different $C_{H_2O_2}$: 3%, 5%, and 8%. The "microraces" shows remarkable speed acceleration (~3 folds) for $C_{H_2O_2}$ increasing from 3 to 10%, which proves that v_j^{ave} is strongly dependent on

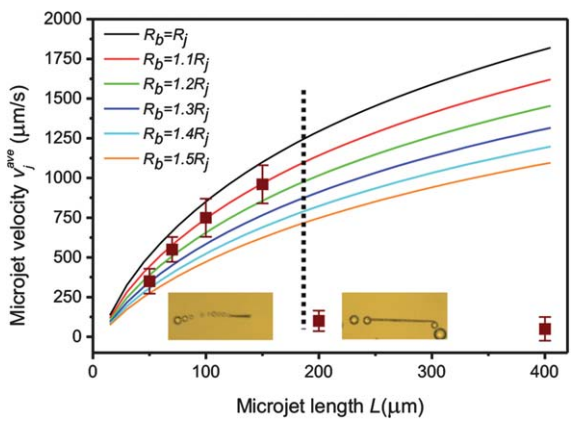

Fig. 4 The average microjet velocity v_j^{ave} *vs.* microjet length L for fixed microjet radius R_j of 10 μm and $C_{H_2O_2}$ of 7%. The solid curves represent bubbles radii R_b with values from R_j to 1.5R_j. The square symbols show v_j^{ave} from our experimental results. The two optical microscope images show the bubble expelling from microjets with different lengths: expelling from one opening for short microjet (left, L = 100 μm) and from both openings for long microjet (right, L = 400 μm).

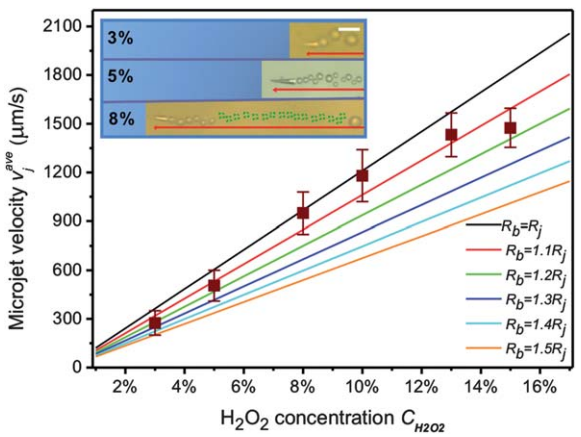

Fig. 5 The average microjet velocity v_j^{ave} *vs.* H_2O_2 concentration $C_{H_2O_2}$ (R_j = 10 μm and L = 100 μm). The solid curves represent bubbles radii R_b with values from R_j to 1.5R_j. The square symbols are derived from our experiment results. The optical microscope images in the inset from *in situ* live video illustrate the moving distance of the microjets in different solutions. The tails behind the microjets can be seen in the images and the dotted circles represent the broken bubbles.

Downloaded by University of California - San Diego on 24 February 2013
Published on 07 November 2011 on http://pubs.rsc.org | doi:10.1039/C1NR10840A

surrounding chemical environment. Since the reaction rate is proportional to the H_2O_2 concentration, the oxygen production and bubble expelling frequency f should be promoted in solution with high $C_{H_2O_2}$. However, we found that the increase of f in high $C_{H_2O_2}$ is accompanied by a slight decrease of bubble radius due to a pressure change under high oxygen production.[13] This deviation is previously neglected in our model and thus a small inconsistency can be observed between experimental and calculated results. As one can see from Fig. 5, the experimental result at $C_{H_2O_2} = 3\%$ fits well with the curve of $R_b = 1.2R_j$, while for $C_{H_2O_2} = 8$ or 10%, the R_b decreases to the value equal to R_j, indicating that the higher gas pressure makes the bubbles become smaller. It is worth noting that with further increase of H_2O_2 concentration to 16%, a tendency to saturation in the experimental microjet velocity can be observed, which may be due to the block of the partial Pt surface by oxygen bubbles under a high oxygen production. This reduces the volume of produced oxygen and correspondingly, the microjet velocity, and even offsets the influence of the radius decrease, leading to an obvious deviation from the linear relationship.

So far, we have demonstrated that the microjet has complex hydrodynamics in an H_2O_2 solution, and that the moving behavior is determined by both microjet geometry and the surrounding chemical environment. If the microjet is employed in future pharmaceuticals and biology, we need to take both factors into consideration when designing the structure of the microjet. In practical application, researchers need to be concerned with not only the absolute value of the velocity but also the ratio between the velocity and dimension of the microengine. Thus, in our case, we focus on how many body lengths (L) the microjet can move in one second. Please note that the relationship between the length and average speed is different from that of the length and the speed by body length. As displayed in Fig. 6, the velocity v_j^{ave} is expressed in the form of body length/s as a function of microjet radius R_j and length L. Here, in order to clearly demonstrate the evolution of the v_j^{ave}, we assume $R_b = R_j$ in the calculation (the value of R_b has little influence in the variation trend of v_j^{ave} as exhibited in Fig. 3, 4, and 5). As one can see, for small R_j, the v_j^{ave} decreases monotonically with increasing L. However, for microjets with a big tubular cavity ($R_j > 30$ μm),

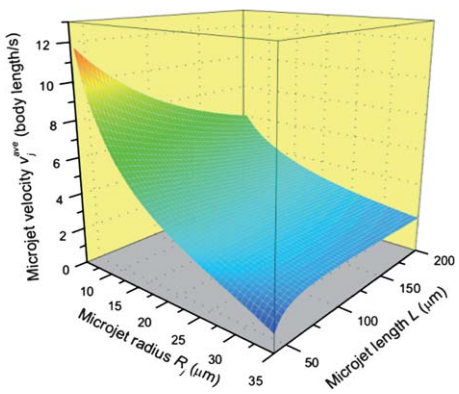

Fig. 6 The average microjet velocity v_j^{ave} as a function of microjet radius R_j and length L ($C_{H_2O_2} = 5\%$). The v_j^{ave} is displayed in the unit of body length/s. To clearly show the variation trend of v_j^{ave}, we assume $R_b = R_j$ in the calculation.

it is interesting to notice an unusual reduction of v_j^{ave} at the small L region, and a maximum value of v_j^{ave} when L is increased from 40 to 200 μm. This means in such a situation (large R_j and small L), the increasing oxygen production with increasing L can balance the effects of both L and $\vec{F}_{jet}$ increases, accelerating the microjet even in terms of body length/s.

Conclusions

In summary, tubular microjets can be self-propelled in an aqueous solution of H_2O_2 due to expelling catalytically generated oxygen bubbles which can be visualized by optical microscopy. To understand the dynamics of the microjet in the solution, we present a model based on the body deformation of the microjet-bubble system and have calculated the average microjet velocity analytically, which is determined by both the geometry of the microjet and the surrounding chemical environment. The calculated results demonstrate that the velocity of the microjet increases linearly with the concentration of hydrogen peroxide. The geometric dimensions of the microjet, such as length and radius, also affect its dynamic characteristics significantly. Good fitting between experimental and calculated results proves the validity of our body-deformation model. Based on this model, we notice that for large and short tubular microcavities a maximum velocity exists in the term of body length/s, which needs to be considered when we make use of the microjet. This work provides deeper insight into the working mechanism of catalytic microjets and the obtained formula is useful in designing micro-/nano-machines for their applications in the pharmaceuticals industry and biology.[29,30] It is worth noting, though, for bio-applications, the bio-compatibility of the microjet should be the major concern. Since the safety of H_2O_2 is concentration based, the H_2O_2 used in our work with concentration up to 8% is not safe for *in vivo* applications. Interestingly, recent work has demonstrated the possibility of using more dilute H_2O_2 solution as the fuel.[16] We believe the future development of chemically powered locomotion of micro-/nanoscale objects should explore new energy rich chemical fuels beyond H_2O_2, which are more bio-friendly, like methanol, formic aid, diazomethane, azides, hydrides, organic peroxides, glucose, and so forth. Initial steps have already been taken recently.[31] Nevertheless, the bubble propulsion mechanism and dynamics of catalytic motion of the microjet, which are the focuses of present work, are of remarkable interest, and may pave the way for future development of micro-/nanomotors propelled by bubble recoiling using biocompatible fuels.

Acknowledgements

The authors thank Zhaoqian Liu and Zhijun Qiu for experimental help. GSH and YFM thank the support from the Natural Science Foundation of China (No. 61008029 and 51102049), Program for New Century Excellent Talents in University (No. NCET-10-0345), Shanghai Pujiang Program (No. 11PJ1400900), and State Key Laboratory of ASIC & System (No. 10KF005). RL acknowledges the support by the Shanghai Municipal of Science and Technology (08QH14002), National Basic Research Program of China (2006CB302703), the Seed Funds for Key Science and Technology Innovation Projects of MOE (708020),

 This journal is © The Royal Society of Chemistry 2011

View Article Online

and the "985" Micro/Nanoelectronics Science and Technology Platform.

Notes and references

1 M. Schliwa and G. Woehlke, *Nature*, 2003, **422**, 759.
2 C. Mavroidis, A. Dubey and M. L. Yarmush, *Annu. Rev. Biomed. Eng.*, 2004, **6**, 363.
3 M. G. L. van den Heuvel and C. Dekker, *Science*, 2007, **317**, 333.
4 R. F. Ismagilov, A. Schwartz, N. Bowden and G. M. Whitesides, *Angew. Chem., Int. Ed.*, 2002, **41**, 652.
5 W. F. Paxton, K. C. Kistler, C. C. Olmeda, A. Sen, S. K. St.Angelo, Y. Cao, T. E. Mallouk, P. E. Lammert and V. H. Crespi, *J. Am. Chem. Soc.*, 2004, **126**, 13424.
6 S. Fournier-Bidoz, A. C. Arsenault, I. Manners and G. A. Ozin, *Chem. Commun.*, 2005, 441.
7 G. A. Ozin, I. Manners, S. Fournier-Bidoz and A. Arsenault, *Adv. Mater.*, 2005, **17**, 3011.
8 D. Kagan, R. Laocharoensuk, M. Zimmerman, C. Clawson, S. Balasubramanian, D. Kang, D. Bishop, S. Sattayasamitsathit, L. Zhang and J. Wang, *Small*, 2010, **6**, 2741.
9 P. Dhar, Th. M. Fischer, Y. Wang, T. E. Mallouk, W. F. Paxton and A. Sen, *Nano Lett.*, 2006, **6**, 66.
10 Y. Wang, R. M. Hernandez, D. J. Bartlett, J. M. Bingham, T. R. Kline, A. Sen and T. E. Mallouk, *Langmuir*, 2006, **22**, 10451.
11 N. I. Kovtyukhova, *J. Phys. Chem. C*, 2008, **112**, 6049.
12 J. G. Gibbs and Y.-P. Zhao, *Appl. Phys. Lett.*, 2009, **94**, 163104.
13 A. A. Solovev, Y. F. Mei, E. B. Urena, G. S. Huang and O. G. Schmidt, *Small*, 2009, **5**, 1688.
14 K. M. Manesh, R. Yuan, M. Clark, D. Kagan, S. Balasubramanian and J. Wang, *ACS Nano*, 2010, **4**, 1799.
15 A. A. Solovev, S. Sanchez, M. Pumera, Y. F. Mei and O. G. Schmidt, *Adv. Funct. Mater.*, 2010, **20**, 2430.
16 S. Sanchez, A. A. Solovev, Y. F. Mei and O. G. Schmidt, *J. Am. Chem. Soc.*, 2010, **132**, 13144.
17 A. A. Solovev, Y. F. Mei and O. G. Schmidt, *Adv. Mater.*, 2010, **22**, 4340.
18 Y. F. Mei, A. A. Solovev, S. Sanchez and O. G. Schmidt, *Chem. Soc. Rev.*, 2011, **40**, 2109.
19 H. C. Berg and R. A. Anderson, *Nature*, 1973, **245**, 380.
20 M. Silverman and M. Simon, *Nature*, 1974, **249**, 73.
21 Y. F. Mei, G. S. Huang, A. A. Solovev, E. Bermúdez Ureña, I. Mönch, F. Ding, T. Reindl, R. K. Y. Fu, P. K. Chu and O. G. Schmidt, *Adv. Mater.*, 2008, **20**, 4085.
22 Y. Chen, K. Peng and Z. Cui, *Microelectron. Eng.*, 2004, **73–74**, 278.
23 O. G. Schmidt and K. Eberl, *Nature*, 2001, **410**, 168.
24 J. G. Gibbs and Y.-P. Zhao, *Small*, 2009, **5**, 2304.
25 E. M. Purcell, *Am. J. Phys.*, 1977, **45**, 3.
26 M. Arora, C. Oh and K. A. Morch, *Phys. Rev. Lett.*, 2004, **92**, 174501.
27 J. Happle and H. Brenner, *Low Reynolds Number Hydrodynamics*, Prentice Hall, Englewood Cliffs, NJ, 1965.
28 A. A. Solovev, S. Sanchez, Y. F. Mei and O. G. Schmidt, *Phys. Chem. Chem. Phys.*, 2011, **13**, 10131.
29 J. Wu, S. Balasubramanian, D. Kagan, K. Manesh, S. Campuzano and J. Wang, *Nature Comm.*, 2010, **1**, 36.
30 D. Kagan, S. Campuzano, S. Balasubramanian, F. Kuralay, G.-U. Flechsig and J. Wang, *Nano Lett.*, 2011, **11**, 2083.
31 D. Pantarotto, W. R. Browne and B. L. Feringa, *Chem. Commun.*, 2008, 1533.

Downloaded by University of California - San Diego on 24 February 2013
Published on 07 November 2011 on http://pubs.rsc.org | doi:10.1039/C1NR10840A

View publication stats